Identifying Reaction Network Structures for Lithium-Ion Battery Cathodes at Thermal-Runaway Onset Temperatures

Mark James Wootton[a,b] and Solomon F. Brown[a,b *]

[a] School of Chemical, Materials, and Biological Engineering, The University of Sheffield, Pam Liversidge Building, Mappin Street, Sheffield, S1 3JD, United Kingdom
[b] The Faraday Institution, Quad One, Harwell Science and Innovation Campus, Didcot, OX11 0RA, United Kingdom
[*] Corresponding Author. *Email*: s.f.brown@sheffield.ac.uk

30th June 2026

Abstract

Lithium-ion batteries undergo a self-sustaining exothermic breakdown process known as thermal runaway when subject to sufficiently high temperatures, presenting a hazard to human health from fire and effluent toxicity, thus demanding the attention of research to minimise these risks. For multitudinous reasons the chemistry of these events is difficult to study by realtime experimental methodologies while underway, so the availability of a theoretical approach to elucidate the mechanisms at play during thermal runaway should be an important supplement to this effort. Here we present a method for the automatic construction of reaction networks for the decomposition of cathodic materials, including approaches for imposing plausibility constraints, achieved via programmatic querying of a public database of chemical species and filtering of results to a manageable volume. The methodology is applied to the cathode species, LFP, LCO, and LMO, for which reaction networks of the cathode decomposition process at a temperature typical of thermal runaway are produced and visualised, with the pathways and decomposition products also tabulated alongside energetic characterisation. There is considerable variation in both the overall complexity of the networks and the proportion of reactions and species discovered in either primary breakdowns or secondary interaction between products of the former.

Keywords: energy storage | battery safety | lithium-ion batteries | thermal runaway | LFP/LCO/LMO cathode decomposition | reaction networks

Nomenclature

LIB lithium-ion battery

LFP lithium iron phosphate ($LiFePO_4$)

NMC lithium nickel cobalt manganese oxide ($LiNi_xMn_yCo_{1-x-y}O_2$)

LCO lithium cobalt oxide ($LiCoO_2$)

LMO lithium manganese oxide ($LiMn_2O_4$)

NCA lithium nickel cobalt aluminium oxide ($LiNi_xCo_yAl_{1-x-y}O_2$)

API Application Programming Interface

MP The Materials Project, see https://www.materialsproject.org

1 Introduction

From the smallest of portable electronic devices to grid-scale energy storage installations, the lithium-ion battery (LIB) has become an indispensable technological advancement since its first economically viable implementation, developed across the mid-1970s to early 1980s by figures such as Whittingham [1], Goodenough [2], and Yoshino [3, 4]. Since this original inception, a plethora of variations

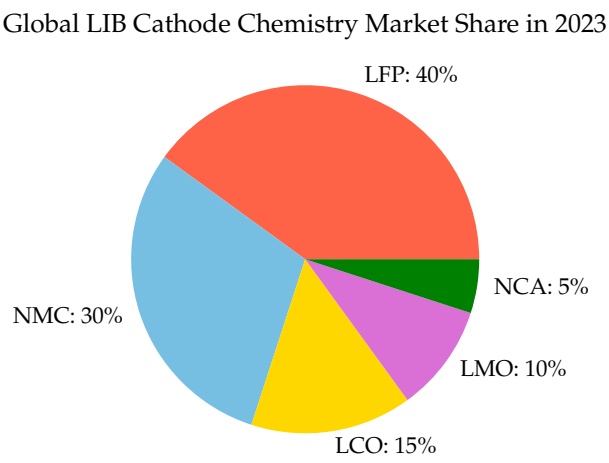


Figure 1: Gravimetric market share of major lithium-ion battery cathode types in 2023 [5] — data provided for general contextualisation in a rapidly evolving sector

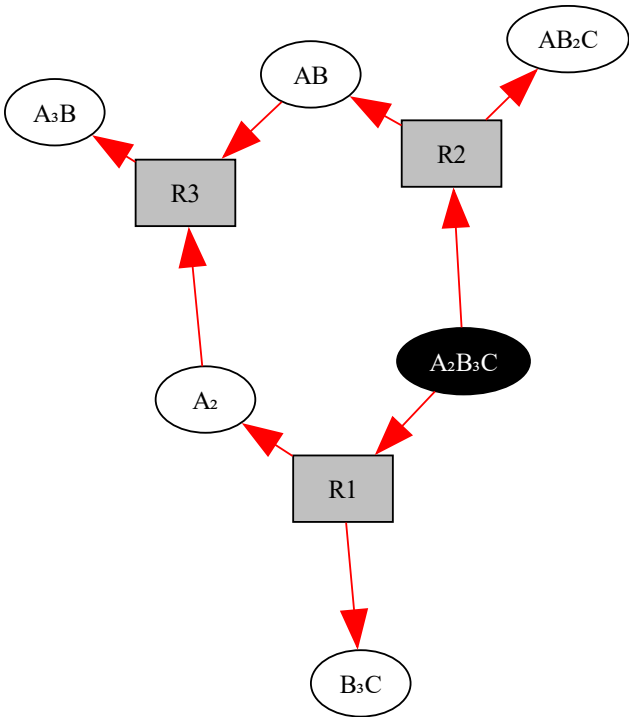


Figure 2: Reaction network representing the example pathways given in equations (1 – 3) for the breakdown of "A_2B_3C".

utilising different lithium-based cathodes have matured to the point of widespread commercial deployment, illustrated in Figure 1. To differing extents with respect to the particular chemistry used, a common issue associated with LIBs is thermal runaway – the self-sustaining exothermic process in which the chemical constitutions of the LIB decompose when a cell reaches temperatures of about 400 K [6]. Aside from the danger posed by the release of heat in and of itself, the resulting gaseous effluent is comprised of toxic and flammable species [7], posing direct hazards to proximal human life. Given that most small-to-medium-scale LIB applications are in close contact with their operator, characterising their chemical decomposition is of considerable interest. In addition to issues of expense and hazard mitigation, efforts to collect empirical data can be difficult, with species of interest being highly reactive and produced at high temperatures [8, 9], *e.g.* hydrogen fluoride (HF) [7], which is particularly corrosive [10] and toxic [11], rendering the endeavour a challenge, even with expensive specialist equipment. It is for this reason that computational methodologies are an important part of the toolkit to set expectations in the study of these materials. Reaction networks are one such tool and create the opportunity to consider the gamut of processes underway in a system that are otherwise difficult to observe [9, 12]; in this case, the decomposition of LIB cathodes at thermal-runaway temperatures. A formal mathematical description of a reaction network can be found in such works as that of Pospíchal and Kvasnička [13], but in brief, they can be explained thus:

A chemical equation describes the change in arrangement of atoms from one initial set of species, *i.e.* the reactants, to another, *i.e.* the products. To describe the interplay of many chemical reactions occurring concurrently and coterminously, a reaction network links a web of species by way of each pathway that can produce or consume them. By illustration, suppose that with A, B, and C as placeholder elements, a species, A_2B_3C, has the decomposition pathways,

$$A_2B_3C \longrightarrow A_2 + B_3C \tag{1}$$

and

$$A_2B_3C \longrightarrow AB + AB_2C\,, \tag{2}$$

with products from equations (1) and (2) reacting, such that,

$$AB + A_2 \longrightarrow A_3B\,. \tag{3}$$

These chemical pathways can thus be presented in reaction network form as seen in Figure 2.

It has been demonstrated by Bugryniec et al. [14] that reaction networks, used in

conjunction with microkinetics [15], can be used in a predictive capacity regarding the decomposition products from LIB electrolytes and their solvents. The structure of their reaction networks was derived by surveying the available literature for studies documenting relevant chemical interactions and aggregating the findings. The drawbacks of this approach are the expenditure of working time in the active search process and the unknown state of extant publications prior to this undertaking.

An alternative approach is to produce the reaction network algorithmically, as was achieved in the literature with examples such as Lee et al. [16]. Working with a selection of organic compounds, the authors used an established set of molecular start and end states, with a large number of possible, but not necessarily probable, intermediaries, implementing a Monte Carlo tree search to select only the pathways most likely to be representative of real-world dynamics. Likewise, Liu and Neelamegham [17] used machine-readable data extracted from the literature in conjunction with the GNAT [18] package for MATLAB to automate the mapping of enzymatic processes as a reaction network. In contrast to a purely data-driven approach, Wen et al. [19] tout the prospect of algorithms that assess the viability of each pathway by way of molecular dynamics [20] or density functional theory (DFT) [21], supplemented with a machine learning process to reduce the volume of calculations required. The body of literature discussed in the review by Unsleber and Reiher [22] showcases various examples of computational methods used to survey data as viable routes to reaction network construction. However, most works cited predominantly serve as a proof-of-concept, with none exceeding complexities on the order of some hundreds of species or some thousands of reaction pathways. The works referenced largely concern themselves with gaseous organic compounds, with some dealing with transition-metal-based systems, and without including further complications, such as the involvement of solvents.

In a similar vein, this work presents reaction networks composed programmatically using an existing catalogue of chemical species, describing the decomposition of LIB cathodes so as to derive insights regarding the processes at play and possibly lay the groundwork for future study by microkinetics. Unlike many of the examples discussed above, these systems are inorganic.

2 Methodology

It is the ambition of this work, through leveraging existing software tools and available data, to construct reaction networks for the decomposition of LIB cathodes, with the aim to produce results that are useful both as a basis for future modelling work and in and of themselves for extracting insights regarding the properties of the system. On both counts, it is therefore important to develop a procedure that yields a tractable body of data and in this section, the process for so gathering and filtering pathways is outlined.

Spearheaded by Kristin Persson, since 2011 the Materials Project (MP) [23–25] has maintained a database of molecules and atomic lattice structures, both observed and hypothetical, numbering almost two hundred thousand entries at the time of writing, detailing chemical parameters and crystallographic characteristics. With the aim of empowering novel discoveries in the material and chemical sciences, particularly battery technology, the data is made highly accessible and numerous software tools are made publicly available, including an API (`mp_api`) [26] to allow programmatic query and retrieval of the properties found in the materials explorer [27–29] and tools for ascertaining stoichiometrically permissible pathways (`rxn_network`) [30, 31], facilitating the construction of reaction networks, as is discussed in the immediate sequel.

The process used for the construction of the reaction network structures in this work was organised as follows, with the process also depicted in flowchart form in Figure 3:

Phase 1. — Direct cathode decomposition:

a. `mp_api` is used to extract the list of all species in the MP-database comprised of the desired elements (*i.e.* any number of said elements, from just one to all of them, may appear in a species and in any ratio. Elements outside the given list are not permitted).

b. Species more than 0.025 eV/atom above the convex hull of stability were removed. This was found to be the practical upper limit imposed by computational tractability.

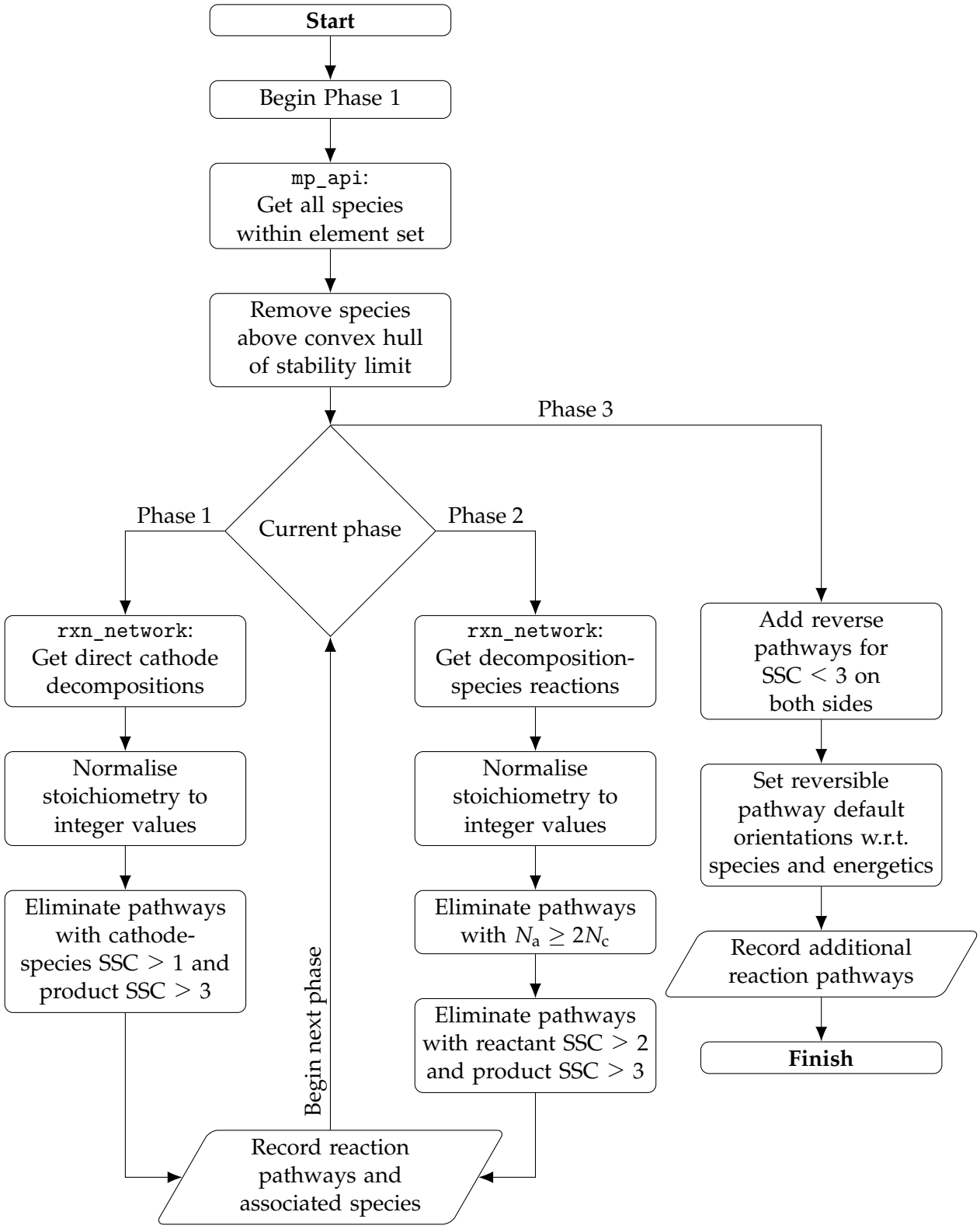


Figure 3: Flowchart describing the reaction network pathway discovery process. Note: "summed stoichiometric coefficients" is abbreviated to "SSC". N_a refers to the number of atoms involved in a pathway and N_c is the number of atoms in cathode species with a stoichiometric coefficient of one.

c. `rxn_network` is then used to calculate all valid reactions between these species, with specified parameters and limitations:
   i. All chemical pathways must start with the cathode species.
   ii. A temperature of 400 K was set, corresponding to typical thermal-runaway onset temperatures [6].

d. As the chemical pathways are returned with fractional stoichiometry, the ratios of species are converted to integers. Any pathways requiring a stoichiometric coefficient greater than one for the cathode species are eliminated and a limit of a total coefficient no greater than three is imposed for the product (*i.e.* 3 A, A + 2 B, or A + C + B are all permissible, for species A, B, and C).

e. The resulting list of reaction pathways and all chemical species featured therein are recorded.

Phase 2. — Decomposition product interaction:

a. The same steps as described in Phase 1 up to part c are repeated using the list of species resulting from the first phase (including the cathode), rather than exclusively the cathode.

b. The same actions as in Phase 1d onwards are taken, but with a total stoichiometric coefficient limit of two for the reactant and three for the product, and an upper limit of $2N_c - 1$ atoms involved in each reaction, where N_c is the number of atoms in the cathode species for a stoichiometric coefficient of one.

Phase 3. — Compilation and final processing:

a. The combined list of reactions across the two phases is then filtered to remove duplicate results.

b. The reverse reaction of pathways where the sum of stoichiometric coefficients is no more than two for both reactant and product are added to the list.

c. The final set of reaction pathways and chemical species are output. For the purposes of presentation in this work, the default directionality of reversible pathways is selected as follows:
   i. If one side contains the cathode species, the default orientation sets this as the reactant(s).
   ii. Otherwise, the side with the greatest sum of stoichiometric coefficients pertaining specifically to species found during Phase 1 is set as the reactant(s).
   iii. In the case of equal standing with respect to the first two criteria, the exothermic orientation is selected in preference to the endothermic counterpart.

The work presented deliberately constrains its scope to retain computational tractability. No species beyond the cathode itself are considered, such as those found in the SEI, electrolyte, or solvent, nor are any species that may ingress from the external environment. No distinction is made between species sharing a chemical formula with differing structures nor within the gamut of possible phases that a species may take, and for species formation energies, the lowest value [1] extracted from the MP database is selected where multiple are returned. Total elemental ratios are always conserved across pathways. Charge is not a criterion in pathway filtering. Reaction products from the first phase are handled in the second phase under the assumption that all are in contact with each other and available to react. Reversibility of reactions [32] is assumed for those meeting the aforementioned criterion, even though for some pathways, the energetics may be such that one direction will be in fact vastly more probable than that of its counterpart.

It should also be acknowledged that as this work relies on a third-party database, its completeness regarding chemical species comprised of the relevant elemental compositions is a potential limiting factor. Whether the breadth of data available varies between the cathode chemistries studied in this work is not explicitly considered in the analysis, but if at a time in the future the MP database is expanded, it may be possible to extract more extensive reaction networks. Not all species in the MP database have been empirically observed but the expectation of stability, or otherwise, is provided. Unstable species are included in the initial analysis and can be thought of as intermediate states.

[1] *i.e.* a negative value of highest magnitude

3 Results

Having established the procedure for generating reaction networks, cathode chemistries must now be selected for its application. The three LIB types chosen for this study are LFP, LCO, and LMO and the methodology was applied as described in Section 2 identically to each of these in turn. As seen in Figure 1, all have notable market share, with LFP being the most common overall. While NMC is more prevalent than the other two, it would introduce additional complications beyond what is preferable for this demonstration; there are several different ratios of Ni, Mn, and Co available [33, 34] and as it is intended to facilitate possible DFT studies, it is desirable to restrict chemical species to integer atom counts within each formula. This would functionally require a starting point of $Li_3Ni_xMn_yCo_{3-x-y}O_6$ (*i.e.* $N_c = 12$), producing a much larger pathway set and substantially more computationally expensive DFT demands. Additionally, even if fractional atomic ratios were permitted, the length of the list of elements in play would also massively increase the number of pathways to be processed; five for NMC, versus four, three, and three for LFP, LCO, and LMO respectively [2]. For the LFP, LCO, and LMO systems, the species found in the decomposition pathway identification process and the chemical equations of these reactions are found in Tables 1 to 3 and Tables 4 to 6, along with properties such as formation energy per atom for the former and reaction energy change for the latter [3]. The reaction energies and species formation energies are plotted in the Figures A.1 to A.3 (see *Appendix*) and the reaction networks themselves are visualised in Figures 4 to 6, with a summary of their properties given in Table 7.

Table 1: Species from LFP-cathode decomposition

	Species	Stable	Atom Count	Formation Energy [eV/atom]
	$LiFePO_4$	✓	7	−2.48
Phase 1	Li	✓	1	0.00
	P	✓	1	0.00
	O_2	✓	2	0.00
	FeO	✓	2	−1.48
	LiFeP	✓	3	−0.65
	PO_3	✗	4	−1.94
	$LiFeO_2$	✓	4	−1.94
	$LiPO_3$	✓	5	−2.70
	$FePO_4$	✓	6	−2.35
Phase 2	Fe	✓	1	0.00
	FeP	✓	2	−0.60
	LiP	✓	2	−0.62
	Fe_2P	✓	3	−0.46
	FeP_2	✓	3	−0.54
	LiFeP	✓	3	−0.65
	Li_2O	✓	3	−2.06
	Li_2O_2	✓	4	−1.65
	Fe_2O_3	✓	5	−1.71
	Li_2FeO_2	✗	5	−1.88
	P_2O_3	✗	5	−1.96
	Li_2FeO_3	✓	6	−1.88
	$Fe(PO_3)_2$	✓	6	−2.47
	P_2O_5	✓	7	−2.45
	Fe_2PO_5	✓	8	−2.18
	$LiFeP_2O_7$	✓	11	−2.53
	$Li_2FeP_2O_7$	✗	12	−2.57

4 Discussion

With an additional element in play (four versus three), the LFP-reaction-network-construction process gives the largest body of results, yielding a total of 59 reactions identified, of which five were direct decompositions of the cathode species in Phase 1 and 54 were Phase 2 reactions between products of Phase 1, compared to nine reactions (two Phase 1 and seven Phase 2) from LCO and five (two Phase 1 and three Phase 2) from LMO [4]. Consistently across the three chemistries, the reactions produced in Phase 1 are universally endothermic, with all exothermic reactions appearing in the results stemming from Phase 2, *i.e.* interactions between cathode-decomposition products. No relation between the magnitude of the reaction energy and the discovery phase was observed. Comparing the exothermic reaction from each chemistry releasing the most energy per atom, R_{30}^{LFP} produced the largest magnitude with R_5^{LMO} and R_8^{LCO} in second and third place respectively. With regard to how many species were first identified in Phase 1 and 2, results were dissimilar for all cases. LFP produced nine species from direct cathode-breakdown, with a further 17 resulting

[2] All of the issues raised *vis-à-vis* NMC also apply to the less-common NCA chemistry.

[3] Reaction energy uncertainty is quoted as reported by `rxn_network` via the extraction of data from the Materials Project

[4] To illustrate the importance of the filtering steps, in the case of LFP, the raw list of reactions discovered numbered 370 from Phase 1 and 1106 from Phase 2.

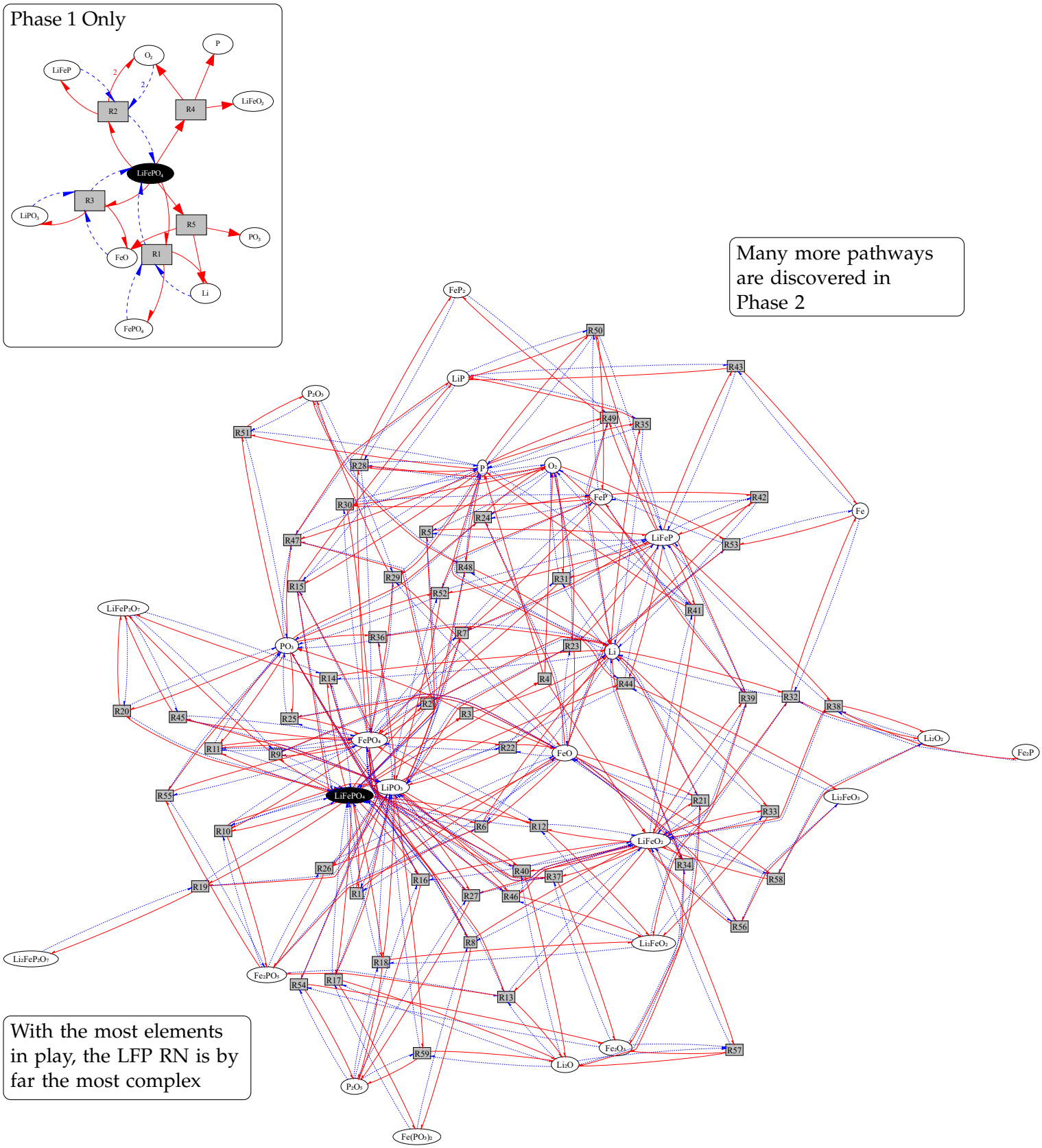


Figure 4: Reaction network for LFP-cathode decomposition. Red solid lines —— and blue dashed lines - - - - respectively mark forward and reverse reaction pathways. Arrowhead orientation indicates reactants; away, and products; towards, with harpoon-style heads ⇀ for reversible pathways and full arrowheads → are used otherwise. Non-unitary stoichiometric coefficients are labelled. Species and pathways are tabulated in Tables 1 and 4.

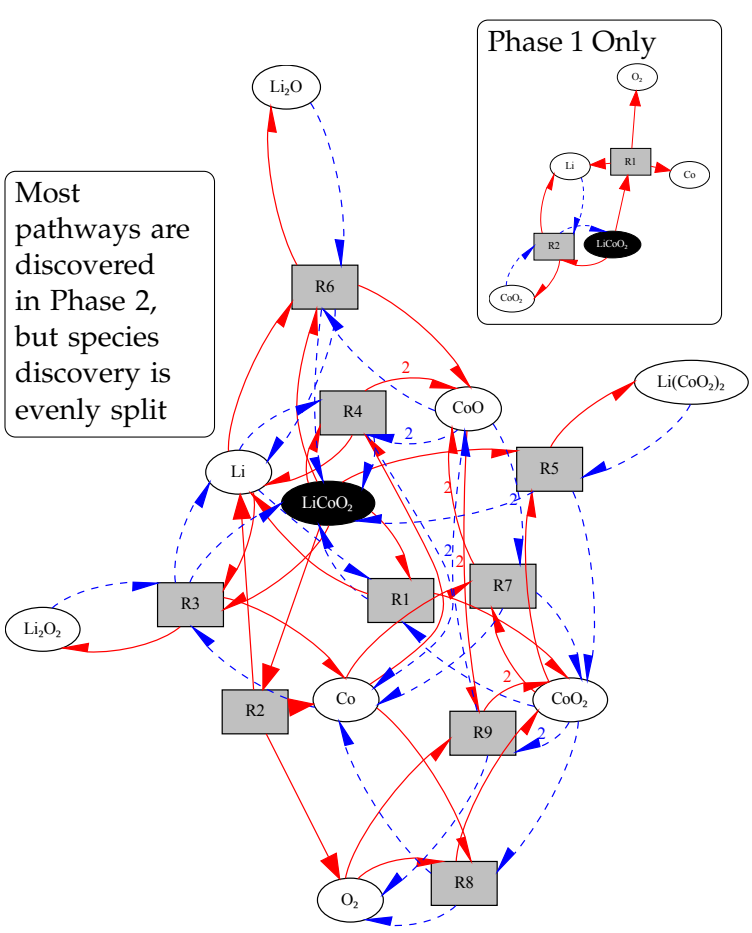


Figure 5: Reaction network structure for LCO-cathode decomposition. Species and pathways are tabulated in Tables 2 and 5.

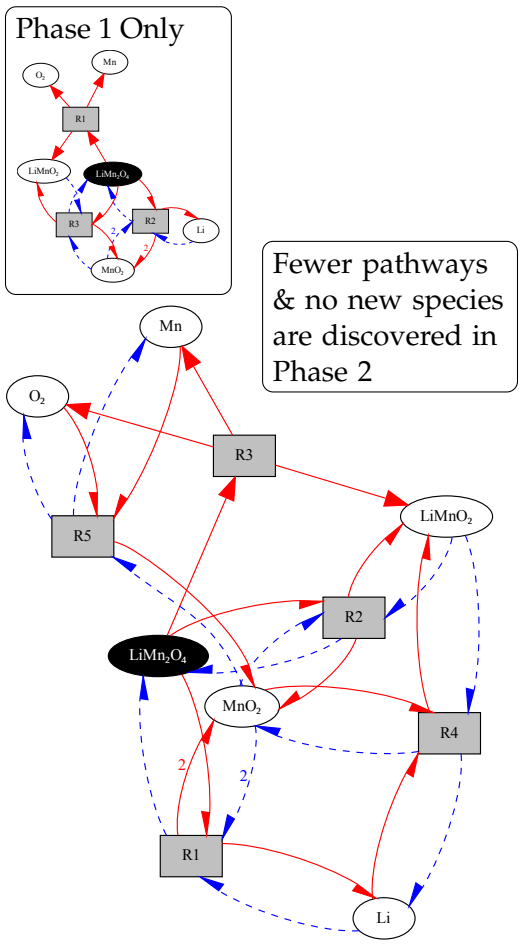


Figure 6: Reaction network for LMO-cathode decomposition. Species and pathways are tabulated in Tables 3 and 6.

Figures 5–6: Red solid lines —— and blue dashed lines - - - - respectively mark forward and reverse reaction pathways. Arrowhead orientation indicates reactants; away, and products; towards, with harpoon-style heads ⇀ for reversible pathways and full arrowheads → are used otherwise. Non-unitary stoichiometric coefficients are labelled.

Table 2: Species from LCO-cathode decomposition

	Species	Stable	Atom Count	Formation Energy [eV/atom]
	$LiCoO_2$	✓	4	−1.75
Phase 1	Li	✓	1	0.00
	Co	✓	1	0.00
	O_2	✓	2	0.00
	CoO_2	✓	3	−1.07
Phase 2	CoO	✓	2	−1.27
	Li_2O	✓	3	−2.06
	Li_2O_2	✓	4	−1.65
	$Li(CoO_2)_2$	✓	5	−1.51

Table 3: Species from LMO-cathode decomposition

	Species	Stable	Atom Count	Formation Energy [eV/atom]
	$LiMn_2O_4$	✓	7	−2.07
Phase 1	Li	✓	1	0.00
	Mn	✓	1	0.00
	O_2	✓	2	0.00
	MnO_2	✓	3	−1.82
	$LiMnO_2$	✓	4	−2.16

only from Phase 2 pathways, for a total of 26. By contrast, an even split of four each was found from the LCO reaction network, and with LMO, not one new species was found in Phase 2, with all five species discovered appearing among Phase 1 products; *i.e.* the products of Phase 2 were all species that also appeared in the direct products of cathode breakdown in Phase 1. For the applicable cases (LFP and LCO) Phase 2 tended to produce larger species, in the sense of a greater number of atoms in the chemical formula, and across all species in all cases, the magnitude of formation energy per atom was generally

Table 4: Reactions in LFP-cathode decomposition, see Figure 4 for visualisation — Part 1 of 2

	Reaction №	Chemical Equation	Atom Count	Forward Energy Change [eV/atom]
Phase 1	R_1^{LFP}	$LiFePO_4 \rightleftharpoons FeO + LiPO_3$	7	0.13 ± 0.06
	R_2^{LFP}	$LiFePO_4 \rightleftharpoons FePO_4 + Li$	7	0.44 ± 0.07
	R_3^{LFP}	$LiFePO_4 \longrightarrow FeO + Li + PO_3$	7	0.91 ± 0.06
	R_4^{LFP}	$LiFePO_4 \longrightarrow LiFeO_2 + O_2 + P$	7	1.26 ± 0.06
	R_5^{LFP}	$LiFePO_4 \rightleftharpoons LiFeP + 2\,O_2$	7	1.99 ± 0.06
Phase 2	R_6^{LFP}	$FeO + LiFePO_4 \rightleftharpoons Fe_2PO_5 + Li$	9	0.31 ± 0.06
	R_7^{LFP}	$FeP + LiFePO_4 \rightleftharpoons FePO_4 + LiFeP$	9	0.27 ± 0.05
	R_8^{LFP}	$FePO_4 + LiFePO_4 \rightleftharpoons Fe(PO_3)_2 + LiFeO_2$	13	0.12 ± 0.05
	R_9^{LFP}	$FePO_4 + LiFePO_4 \rightleftharpoons FeO + LiFeP_2O_7$	13	0.06 ± 0.06
	R_{10}^{LFP}	$FePO_4 + LiFePO_4 \rightleftharpoons Fe_2PO_5 + LiPO_3$	13	0.05 ± 0.05
	R_{11}^{LFP}	$LiFePO_4 + PO_3 \rightleftharpoons FePO_4 + LiPO_3$	11	-0.22 ± 0.05
	R_{12}^{LFP}	$LiFeO_2 + LiFePO_4 \rightleftharpoons FePO_4 + Li_2FeO_2$	11	0.14 ± 0.05
	R_{13}^{LFP}	$LiFeO_2 + LiFePO_4 \rightleftharpoons Fe_2PO_5 + Li_2O$	11	0.14 ± 0.05
	R_{14}^{LFP}	$LiFePO_4 + LiPO_3 \rightleftharpoons Li + LiFeP_2O_7$	12	0.25 ± 0.06
	R_{15}^{LFP}	$LiFePO_4 + P \rightleftharpoons FePO_4 + LiP$	8	0.27 ± 0.06
	R_{16}^{LFP}	$LiFePO_4 + PO_3 \rightleftharpoons LiFeO_2 + P_2O_5$	11	0.19 ± 0.04
	R_{17}^{LFP}	$LiFePO_4 + LiPO_3 \rightleftharpoons Fe(PO_3)_2 + Li_2O$	12	0.20 ± 0.05
	R_{18}^{LFP}	$LiFePO_4 + LiPO_3 \rightleftharpoons Li_2FeO_2 + P_2O_5$	12	0.50 ± 0.04
	R_{19}^{LFP}	$LiFePO_4 + LiPO_3 \rightleftharpoons Li_2FeP_2O_7$	12	-0.01 ± 0.06
	R_{20}^{LFP}	$LiFePO_4 + PO_3 \rightleftharpoons LiFeP_2O_7$	11	-0.22 ± 0.06
	R_{21}^{LFP}	$FeO + LiFeO_2 \rightleftharpoons Fe_2O_3 + Li$	6	0.34 ± 0.06
	R_{22}^{LFP}	$FePO_4 + Li \rightleftharpoons FeO + LiPO_3$	7	-0.31 ± 0.06
	R_{23}^{LFP}	$LiFeP + 2\,O_2 \rightleftharpoons FeO + LiPO_3$	7	-1.86 ± 0.05
	R_{24}^{LFP}	$FeO + PO_3 \rightleftharpoons FeP + 2\,O_2$	6	1.38 ± 0.05
	R_{25}^{LFP}	$FeO + PO_3 \rightleftharpoons FePO_4$	6	-0.54 ± 0.06
	R_{26}^{LFP}	$FeO + FePO_4 \rightleftharpoons Fe_2PO_5$	8	-0.04 ± 0.06
	R_{27}^{LFP}	$FePO_4 + LiPO_3 \rightleftharpoons LiFeO_2 + P_2O_5$	11	0.40 ± 0.04
	R_{28}^{LFP}	$FePO_4 + P \rightleftharpoons FeP_2 + 2\,O_2$	7	1.60 ± 0.06
	R_{29}^{LFP}	$FePO_4 + P \rightleftharpoons FeO + P_2O_3$	7	-0.07 ± 0.05

Continued on page 11

positively correlated with the atom count.

As remarked above, the reaction network for LFP decomposition, seen in Figure 4, is the most complex. This follows as a result of the increased number of chemical elements in play, with the four found in LFP permitting much greater variety than the three found in LCO or LMO.

Aside from the properties already discussed, `mp_api` also flags the stability of the species in its database and in Table 1 it is seen that four of the species featured are marked as innately unstable, with one from Phase 1 and three from Phase 2. If pathways featuring these are excluded, the reaction network is reduced to 40 pathways, and this revised version is seen in Figure 7.

Regarding the implications for thermal-runaway hazards, it is observed that there is a significant difference in the distribution of exothermic and endothermic reactions between the second phase pathways for LFP compared to those from LCO and LMO. In the latter instances, exothermic reactions dominate, with a supermajority for LCO and a totality for LMO results. By contrast, a near-even split is seen for LFP, with slightly more endothermic reactions than exothermic. It is additionally seen that the LFP pathways produce the species with the greatest magnitude of formation energy, with six of its stable species exceeding that of any of the chemical products of the LCO or LMO systems. Considering both observations, with all other things being equal with respect to *in-situ* pathway probability, this would seem to be consistent with the observed performance of LFP pertaining to its reduced propensity towards thermal-runaway onset [35] as it would imply that energy has more opportunities to be absorbed by these chemical processes in the formation of the species with

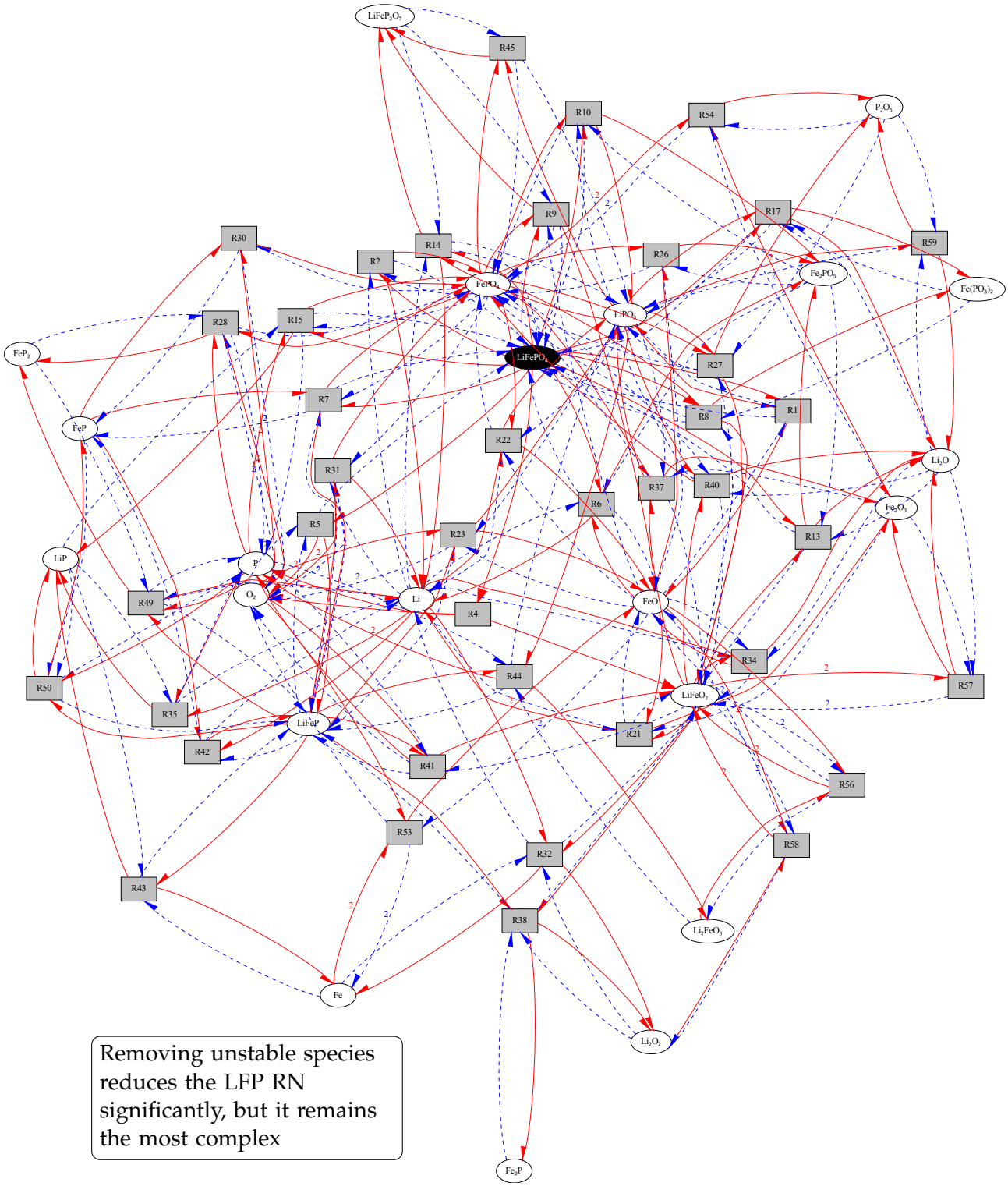


Figure 7: Reaction network for LFP-cathode decomposition, reduced from the version seen in Figure 4 by the removal of pathways containing unstable chemical species. Red solid lines —— and blue dashed lines - - - - respectively mark forward and reverse reaction pathways. Arrowhead orientation indicates reactants; away, and products; towards, with harpoon-style heads ⇀ for reversible pathways and full arrowheads → are used otherwise. Non-unitary stoichiometric coefficients are labelled. Species and pathways are tabulated in Tables 1 and 4.

Table 4: Reactions in LFP-cathode decomposition, see Figure 4 for visualisation — Part 2 of 2

Continued from page 9

	Reaction №	Chemical Equation	Atom Count	Forward Energy Change [eV/atom]
Phase 2	R_{30}^{LFP}	$FeP + 2\,O_2 \rightleftharpoons FePO_4$	6	-1.92 ± 0.06
	R_{31}^{LFP}	$LiFeP + 2\,O_2 \rightleftharpoons FePO_4 + Li$	7	-1.55 ± 0.06
	R_{32}^{LFP}	$Li + LiFeO_2 \rightleftharpoons Fe + Li_2O_2$	5	0.24 ± 0.04
	R_{33}^{LFP}	$Li + LiFeO_2 \rightleftharpoons Li_2FeO_2$	5	-0.31 ± 0.06
	R_{34}^{LFP}	$Li + LiFeO_2 \rightleftharpoons FeO + Li_2O$	5	-0.26 ± 0.05
	R_{35}^{LFP}	$Li + P \rightleftharpoons LiP$	2	-0.46 ± 0.06
	R_{36}^{LFP}	$Li + PO_3 \rightleftharpoons LiPO_3$	5	-1.09 ± 0.06
	R_{37}^{LFP}	$FePO_4 + LiFeO_2 \rightleftharpoons Fe_2O_3 + LiPO_3$	10	-0.01 ± 0.05
	R_{38}^{LFP}	$LiFeO_2 + LiFeP \rightleftharpoons Fe_2P + Li_2O_2$	7	0.24 ± 0.04
	R_{39}^{LFP}	$LiFeO_2 + LiFeP \rightleftharpoons FeP + Li_2FeO_2$	7	-0.13 ± 0.05
	R_{40}^{LFP}	$LiFeO_2 + LiPO_3 \rightleftharpoons FePO_4 + Li_2O$	9	0.10 ± 0.05
	R_{41}^{LFP}	$LiFeP + O_2 \rightleftharpoons LiFeO_2 + P$	5	-1.02 ± 0.05
	R_{42}^{LFP}	$FeP + Li \rightleftharpoons LiFeP$	3	-0.23 ± 0.06
	R_{43}^{LFP}	$LiFeP \rightleftharpoons Fe + LiP$	3	0.29 ± 0.06
	R_{44}^{LFP}	$LiFeP + LiPO_3 \rightleftharpoons Li_2FeO_3 + 2\,P$	8	0.52 ± 0.05
	R_{45}^{LFP}	$FePO_4 + LiPO_3 \rightleftharpoons LiFeP_2O_7$	11	-0.01 ± 0.06
	R_{46}^{LFP}	$LiFeO_2 + LiPO_3 \rightleftharpoons Li_2FeO_2 + PO_3$	9	0.43 ± 0.05
	R_{47}^{LFP}	$LiPO_3 + P \rightleftharpoons LiP + PO_3$	6	0.76 ± 0.06
	R_{48}^{LFP}	$LiPO_3 + P \rightleftharpoons Li + P_2O_3$	6	0.28 ± 0.04
	R_{49}^{LFP}	$LiFeP + P \rightleftharpoons FeP_2 + Li$	4	0.08 ± 0.06
	R_{50}^{LFP}	$LiFeP + P \rightleftharpoons FeP + LiP$	4	-0.06 ± 0.05
	R_{51}^{LFP}	$P + PO_3 \rightleftharpoons P_2O_3$	5	-0.75 ± 0.04
	R_{52}^{LFP}	$LiFeP + PO_3 \rightleftharpoons FeP + LiPO_3$	7	-0.68 ± 0.05
	R_{53}^{LFP}	$O_2 + 2\,Fe \rightleftharpoons 2\,FeO$	4	-1.28 ± 0.06
	R_{54}^{LFP}	$2\,FePO_4 \rightleftharpoons Fe_2O_3 + P_2O_5$	12	0.36 ± 0.05
	R_{55}^{LFP}	$Fe_2PO_5 + PO_3 \rightleftharpoons 2\,FePO_4$	12	-0.25 ± 0.06
	R_{56}^{LFP}	$FeO + Li_2FeO_3 \rightleftharpoons 2\,LiFeO_2$	8	-0.16 ± 0.06
	R_{57}^{LFP}	$2\,LiFeO_2 \rightleftharpoons Fe_2O_3 + Li_2O$	8	0.10 ± 0.06
	R_{58}^{LFP}	$Li_2O_2 + 2\,FeO \rightleftharpoons 2\,LiFeO_2$	8	-0.37 ± 0.06
	R_{59}^{LFP}	$2\,LiPO_3 \rightleftharpoons Li_2O + P_2O_5$	10	0.54 ± 0.05

the greatest thermodynamic stability, rather than contributing to the heat energy of the system available to drive further decomposition.

5 Conclusions

In this work, reaction networks describing the decomposition pathways of three common variants of cathode found in lithium-ion batteries are presented with the methodology used to derive them. Along with the reactions themselves, the set of chemical species produced is tabulated. As discussed, one of the great challenges for scientific investigation of this topic is the inaccessibility of the reaction products from thermal runaway in realtime, but with the benefit of specific predictions, experimental configuration can be devised with informed expectations of reasonable search parameters. If desired or necessary, the process outlined in this work could be iterated to extract tertiary and quaternary reactions, and indeed arbitrarily many, limited only by time and computational resources.

As reaction dynamics on this timescale should be expected to be dominated by pathways with the most favourable energy barriers, rather than simple thermodynamic feasibility, a useful continuation of this work would be to generate expected reaction rates by analysis of activation energies and transition-state configurations. This would require constructing molecular-scale representations of each chemical species and pathway interaction in a format suitable for DFT calculations. Some interactions could thus be eliminated as functionally implausible and, for the remainder, this would provide the

Table 5: Reactions in LCO-cathode decomposition, see Figure 5 for visualisation

	Reaction №	Chemical Equation	Atom Count	Forward Energy Change [eV/atom]
Phase 1	R_1^{LCO}	$LiCoO_2 \rightleftharpoons CoO_2 + Li$	4	0.86 ± 0.06
	R_2^{LCO}	$LiCoO_2 \longrightarrow Co + Li + O_2$	4	1.52 ± 0.06
Phase 2	R_3^{LCO}	$Li + LiCoO_2 \rightleftharpoons Co + Li_2O_2$	5	0.07 ± 0.04
	R_4^{LCO}	$Co + LiCoO_2 \rightleftharpoons Li + 2\,CoO$	5	0.34 ± 0.06
	R_5^{LCO}	$CoO_2 + LiCoO_2 \rightleftharpoons Li(CoO_2)_2$	7	-0.02 ± 0.06
	R_6^{LCO}	$Li + LiCoO_2 \rightleftharpoons CoO + Li_2O$	5	-0.34 ± 0.05
	R_7^{LCO}	$Co + CoO_2 \rightleftharpoons 2\,CoO$	4	-0.43 ± 0.06
	R_8^{LCO}	$Co + O_2 \rightleftharpoons CoO_2$	3	-0.88 ± 0.06
	R_9^{LCO}	$O_2 + 2\,CoO \rightleftharpoons 2\,CoO_2$	6	-0.15 ± 0.06

Table 6: Reactions in LMO-cathode decomposition, see Figure 6 for visualisation

	Reaction №	Chemical Equation	Atom Count	Forward Energy Change [eV/atom]
Phase 1	R_1^{LMO}	$LiMn_2O_4 \rightleftharpoons Li + 2\,MnO_2$	7	0.48 ± 0.07
	R_2^{LMO}	$LiMn_2O_4 \rightleftharpoons LiMnO_2 + MnO_2$	7	0.05 ± 0.06
	R_3^{LMO}	$LiMn_2O_4 \longrightarrow LiMnO_2 + Mn + O_2$	7	0.72 ± 0.06
Phase 2	R_4^{LMO}	$Li + MnO_2 \rightleftharpoons LiMnO_2$	4	-0.76 ± 0.06
	R_5^{LMO}	$Mn + O_2 \rightleftharpoons MnO_2$	3	-1.57 ± 0.06

Table 7: Summary of the number of reaction pathways and product species appearing in the reaction networks for LIB-cathode decomposition visualised in Figures 4 – 6.

Cathode	Phase 1		Phase 2		Total		Max Energy Release [eV/atom]	
	Products	Pathways	Products	Pathways	Products	Pathways	Products [5]	Pathways
LFP	9	5	17	54	26	59	-0.22 ($\rightarrow LiPO_3$)	-1.92 (R_{30}^{LFP})
LCO	4	2	4	7	8	9	-0.31 ($\rightarrow Li_2O$)	-0.88 (R_8^{LCO})
LMO	5	2	0	3	5	5	-0.09 ($\rightarrow LiMnO_2$)	-1.57 (R_5^{LMO})

reaction rate constants required for microkinetic simulation of the evolving proportions of each species during the cathode-breakdown process. Likewise, it may then become possible to eliminate species on grounds of insufficient stability or formation plausibility, beyond what was achievable in this work. However, such an effort may present a number of challenges; unlike similar exercises, for example, the work undertaken by Bugryniec et al. [14], where the set of species in the study was largely confined to organic compounds, of which it was appropriate to speak in terms of discrete molecules, many of the species featured in this study take the form of solids with a periodic crystalline structure, including the cathode materials themselves. Concordantly, any calculation of their energetics cannot avoid consideration of the interactions resulting from the interatomic bulk. Attempting to treat any of these species as discrete molecules will at best result in an assemblage that can never converge to a physically representative form. While this is not an entirely intractable problem, correct handling will necessitate careful consideration and likely also a relatively substantial expenditure of computational resources. It is also possible that a treatment utilising molecular dynamics with an interatomic potential well suited for chemical interactions may provide a solution to this issue, although not necessarily to the same fidelity as could be achieved via DFT under ideal circumstances. Regardless of which approach is taken in future research, the results presented in this work should provide a helpful initial estimate of which pathways should first be considered from a computational perspective and of which chemical species might be expected in the products of experimental studies of thermal runaway in LIBs. Realtime experimental observation of the chemical evolution of these systems remains a substantial challenge for the time being, but if practical means to perform such work are devised, this would provide a highly

[5] Given as the difference in formation energy of product relative to the cathode species

direct opportunity for empirical validation.

This work has focussed specifically on the cathode materials themselves, but other components of the battery system have important roles in the process of thermal runaway. In particular, the solvents used to permit the mobility of the electrolyte salts are frequently comprised of highly flammable hydrocarbons [14, 36], and SEI compounds undergo exothermic thermal decomposition at temperatures similar to those discussed above [36–38]. Indubitably, both the chemical species and energy released by these will have an impact on the decomposition of the cathode and the subsequent chemical reactions that become possible when the products of the latter come into contact with the former, not to mention the influence of structural components or environmental exposure once internal containment is compromised. An avenue for future work may take the form of the construction of a combined reaction network that incorporates pathways from all parts of the system, although such a study will be considerably more demanding in terms of computational resources.

The results presented are consistent with the known properties of the cathodes studied pertaining to thermal runaway. With the possibility of the invention of novel battery chemistries in the future, it is hoped that the methodology described in this work may be used to contribute to the overall effort to assess the safety of such technologies prior to their widespread deployment.

CRediT authorship contribution statement

Mark James Wootton: Conceptualisation, Methodology, Software, Visualisation, Writing – original draft. **Solomon F. Brown:** Supervision, Writing – review & editing

Orcid ID

Mark James Wootton: 0000-0001-6850-5978
Solomon F. Brown: 0000-0001-8229-8004

Declaration of competing interest

The authors declare that they have no known competing financial interests or personal relationships that could have appeared to influence the work reported in this paper.

Acknowledgements

This research was supported by the Faraday Institution *SafeBatt* project [39] [grant numbers: `FIRG061` and `FIRG086`]. The authors would like to thank Sergio Vernuccio for useful and informative conversations during the conceptualisation of this work, as well as fellow members of *the Brown Group* [40] for feedback during the preparation of this manuscript. Additional gratitude is expressed to the authors of the software packages `Graphviz` [41] and `matplotlib` [42, 43], used in the production of figures in this work.

References

[1] M. S. Whittingham. Electrical Energy Storage and Intercalation Chemistry. *Science*, 192(4244):1126–1127, June 1976. ISSN 1095-9203. doi: 10.1126/science.192.4244.1126.

[2] K. Mizushima, P.C. Jones, P.J. Wiseman, and J.B. Goodenough. Li_xCoO_2 ($0<x\leq1$): A new cathode material for batteries of high energy density. *Materials Research Bulletin*, 15(6): 783–789, June 1980. ISSN 0025-5408. doi: 10.1016/0025-5408(80)90012-4.

[3] A. Yoshino and K. Sanechika. Japanese patent application: 1985-127669, 1985.

[4] Akira Yoshino. The Birth of the Lithium-Ion Battery. *Angewandte Chemie International Edition*, 51(24):5798–5800, February 2012. ISSN 1521-3773. doi: 10.1002/anie.201105006.

[5] Verified Market Reports. Cathode Active Materials for Lithium-ion Batteries Market Size, Industry Expansion & Forecast, 2025. URL `https://www.verifiedmarketreports.com/product/cathode-active-materials-for-lithium-ion-batteries-market`. Report ID: 739626. Accessed: 2025-08-13. *Note: It was confirmed via email that the figures presented pertained specifically to mass of LIBs deployed.*

[6] Yixin Dai and Aidin Panahi. Thermal runaway process in lithium-ion batteries: A review. *Next Energy*, 6:100186, January 2025. ISSN 2949-821X. doi: 10.1016/j.nxener.2024.100186.

[7] Mingming Qiu, Jianghong Liu, Beihua Cong, and Yan Cui. Research Progress in Thermal Runaway Vent Gas Characteristics of Li-Ion Battery. *Batteries*, 9(8):411, August 2023. ISSN 2313-0105. doi: 10.3390/batteries9080411.

[8] Fredrik Larsson, Petra Andersson, Per Blomqvist, Anders Lorén, and Bengt-Erik Mellander. Characteristics of lithium-ion batteries during fire tests. *Journal of Power Sources*, 271:414–420, December 2014. ISSN 0378-7753. doi: 10.1016/j.jpowsour.2014.08.027.

[9] Xuning Feng, Siqi Zheng, Dongsheng Ren, Xiangming He, Li Wang, Hao Cui, Xiang Liu, Changyong Jin, Fangshu Zhang, Chengshan Xu, Hungjen Hsu, Shang Gao, Tianyu Chen, Yalun Li, Tianze Wang, Hao Wang, Maogang Li, and Minggao Ouyang. Investigating the thermal runaway mechanisms of lithium-ion batteries based on thermal analysis database. *Applied Energy*, 246:53–64, July 2019. ISSN 0306-2619. doi: 10.1016/j.apenergy.2019.04.009.

[10] J. R. Crum, G. D. Smith, M. J. McNallan, and S. Hirnyj. Characterization of Corrosion Resistant Materials in Low and High Temperature HF Environments. volume CORROSION 1999 of *NACE International Annual Conference*, pages 1–11, 04 1999. doi: 10.5006/C1999-99382.

[11] Rachel Krebs, Jeffery Owens, and Heather Luckarift. Formation and detection of hydrogen fluoride gas during fire fighting scenarios. *Fire Safety Journal*, 127:103489, January 2022. ISSN 0379-7112. doi: 10.1016/j.firesaf.2021.103489.

[12] Puneet Jindal and Jishnu Bhattacharya. Review—Understanding the Thermal Runaway Behavior of Li-Ion Batteries through Experimental Techniques. *Journal of The Electrochemical Society*, 166(10): A2165–A2193, 2019. ISSN 1945-7111. doi: 10.1149/2.1381910jes.

[13] Jiří Pospíchal and Vladimír Kvasnička. Reaction graphs and a construction of reaction networks. *Theoretica Chimica Acta*, 76(6):423–435, November 1990. ISSN 1432-2234. doi: 10.1007/bf00528881.

[14] Peter J. Bugryniec, Sergio Vernuccio, and Solomon F. Brown. Towards a micro-kinetic model of Li-ion battery thermal runaway — Reaction network analysis of dimethyl carbonate thermal decomposition. *Journal of Power Sources*, 580:233394, October 2023. ISSN 0378-7753. doi: 10.1016/j.jpowsour.2023.233394.

[15] Ivo A. W. Filot. *Introduction to Microkinetic Modeling*. Eindhoven University of Technology, version 1.9.0 edition, 2025. ISBN 978-90-386-5573-4.

[16] Kyunghoon Lee, Jin Woo Kim, and Woo Youn Kim. Efficient Construction of a Chemical Reaction Network Guided By a Monte Carlo Tree Search. *ChemSystemsChem*, 2(5), March 2020. ISSN 2570-4206. doi: 10.1002/syst.201900057.

[17] Gang Liu and Sriram Neelamegham. A Computational Framework for the Automated Construction of Glycosylation Reaction Networks. *PLoS ONE*, 9(6): e100939, June 2014. ISSN 1932-6203. doi: 10.1371/journal.pone.0100939.

[18] Gang Liu, Apurv Puri, and Sriram Neelamegham. Glycosylation Network Analysis Toolbox: a MATLAB-based environment for systems glycobiology. *Bioinformatics*, 29(3):404–406, December 2012. ISSN 1367-4803. doi: 10.1093/bioinformatics/bts703.

[19] Mingjian Wen, Evan Walter Clark Spotte-Smith, Samuel M. Blau, Matthew J. McDermott, Aditi S. Krishnapriyan, and Kristin A. Persson. Chemical reaction networks and opportunities for machine learning. *Nature Computational Science*, 3(1): 12–24, January 2023. ISSN 2662-8457. doi: 10.1038/s43588-022-00369-z.

[20] Kurt Binder, Jürgen Horbach, Walter Kob, Wolfgang Paul, and Fathollah Varnik. Molecular dynamics simulations. *Journal of Physics: Condensed Matter*, 16(5):S429–S453, January 2004. ISSN 1361-648X. doi: 10.1088/0953-8984/16/5/006.

[21] David S. Sholl and Janice A. Steckel. *Density Functional Theory: A Practical Introduction*. Wiley, 2009. ISBN 978-0-470-37317-0.

[22] Jan P. Unsleber and Markus Reiher. The Exploration of Chemical Reaction Networks. *Annual Review of Physical Chemistry*, 71(1):121–142, April 2020. ISSN 1545-1593. doi: 10.1146/annurev-physchem-071119-040123.

[23] MaterialsProject. Materials Project. URL `https://www.materialsproject.org`.

[24] Anubhav Jain, Shyue Ping Ong, Geoffroy Hautier, Wei Chen, William Davidson Richards, Stephen Dacek, Shreyas Cholia, Dan Gunter, David Skinner, Gerbrand Ceder, and Kristin A. Persson. Commentary: The Materials Project: A materials genome approach to accelerating materials innovation. *APL Materials*, 1(1), July 2013. ISSN 2166-532X. doi: 10.1063/1.4812323.

[25] Matthew K. Horton, Patrick Huck, Ruo Xi Yang, Jason M. Munro, Shyam Dwaraknath, Alex M. Ganose, Ryan S. Kingsbury, Mingjian Wen, Jimmy X. Shen, Tyler S. Mathis, Aaron D. Kaplan, Karlo Berket, Janosh Riebesell, Janine George, Andrew S. Rosen, Evan W. C. Spotte-Smith, Matthew J. McDermott, Orion A. Cohen, Alex Dunn, Matthew C. Kuner, Gian-Marco Rignanese, Guido Petretto, David Waroquiers, Sinead M. Griffin, Jeffrey B. Neaton, Daryl C. Chrzan, Mark Asta, Geoffroy Hautier, Shreyas Cholia, Gerbrand Ceder, Shyue Ping Ong, Anubhav Jain, and Kristin A. Persson. Accelerated data-driven materials science with the Materials Project. *Nature Materials*, July 2025. ISSN 1476-4660. doi: 10.1038/s41563-025-02272-0.

[26] Materials Project. The Materials Project API. GitHub repository. URL `https://www.github.com/materialsproject/api`.

[27] Arunima K. Singh, Lan Zhou, Aniketa Shinde, Santosh K. Suram, Joseph H. Montoya, Donald Winston, John M. Gregoire, and Kristin A. Persson. Electrochemical Stability of Metastable Materials. *Chemistry of Materials*, 29(23): 10159–10167, November 2017. ISSN 1520-5002. doi: 10.1021/acs.chemmater.7b03980.

[28] Anjli M. Patel, Jens K. Nørskov, Kristin A. Persson, and Joseph H. Montoya. Efficient Pourbaix diagrams of many-element compounds. *Physical Chemistry Chemical Physics*, 21(45):25323–25327, 2019. ISSN 1463-9084. doi: 10.1039/c9cp04799a.

[29] Kristin A. Persson, Bryn Waldwick, Predrag Lazic, and Gerbrand Ceder. Prediction of solid-aqueous equilibria: Scheme to combine first-principles calculations of solids with experimental aqueous states. *Physical Review B*, 85 (23), June 2012. ISSN 1550-235X. doi: 10.1103/physrevb.85.235438.

[30] Matthew J. McDermott, Shyam S. Dwaraknath, and Kristin A. Persson. A graph-based network for predicting chemical reaction pathways in solid-state materials synthesis. *Nature Communications*, 12(1), May 2021. ISSN 2041-1723. doi: 10.1038/s41467-021-23339-x.

[31] Matthew J. McDermott (`@mattmcdermott`). reaction➔network. GitHub repository. URL `https://www.github.com/materialsproject/reaction-network`.

[32] Jim Pfaendtner and Linda J. Broadbelt. Mechanistic Modeling of Lubricant Degradation. 1. Structure–Reactivity Relationships for Free-Radical Oxidation. *Industrial & Engineering Chemistry Research*, 47(9):2886–2896, March 2008. ISSN 1520-5045. doi: 10.1021/ie0714807.

[33] Johannes Kasnatscheew, Stephan Röser, Markus Börner, and Martin Winter. Do Increased Ni Contents in $LiNi_xMn_yCo_zO_2$ (NMC) Electrodes Decrease Structural and Thermal Stability of Li Ion Batteries? A Thorough Look by Consideration of the Li^+ Extraction Ratio. *ACS Applied Energy Materials*, 2(11):7733–7737, October 2019. ISSN 2574-0962. doi: 10.1021/acsaem.9b01440.

[34] Aurora Gomez-Martin, Friederike Reissig, Lars Frankenstein, Marcel Heidbüchel, Martin Winter, Tobias Placke, and Richard Schmuch. Magnesium Substitution in Ni-Rich NMC Layered Cathodes for High-Energy Lithium Ion Batteries. *Advanced Energy Materials*, 12(8), January 2022. ISSN 1614-6840. doi: 10.1002/aenm.202103045.

[35] Christian Julien, Alain Mauger, Karim Zaghib, and Henri Groult. Comparative issues of cathode materials for li-ion batteries. *Inorganics*, 2(1):132–154, March 2014. ISSN 2304-6740. doi: 10.3390/inorganics2010132.

[36] A. Swiderska-Mocek, P. Jakobczyk, E. Rudnicka, and A. Lewandowski. Flammability parameters of lithium-ion battery electrolytes. *Journal of Molecular Liquids*, 318:113986, November 2020. ISSN 0167-7322. doi: 10.1016/j.molliq.2020.113986.

[37] Languang Lu, Xuebing Han, Jianqiu Li, Jianfeng Hua, and Minggao Ouyang. A review on the key issues for lithium-ion battery management in electric vehicles. *Journal of Power Sources*, 226:272–288, March 2013. ISSN 0378-7753. doi: 10.1016/j.jpowsour.2012.10.060.

[38] Ayushi Mehrotra, Pragya Berwal, Yejun Lee, and Jack J. Yoh. Anode-triggered thermal runaway in $LiFePO_4$ cells under rapid heating: rethinking interfacial stability. *Journal of Power Sources*, 657:238165, November 2025. ISSN 0378-7753. doi: 10.1016/j.jpowsour.2025.238165.

[39] SafeBatt. SafeBatt – The Science of Battery Safety. URL `https://www.safebatt.ac.uk`.

[40] BrownGroup. The Brown Group. URL `https://www.browngroupsheffield.com`.

[41] graphviz. Graphviz - Graph Visualization Tools. URL `https://www.graphviz.org`.

[42] matplotlib. Matplotlib: Visualization with Python. URL `https://matplotlib.org`.

[43] J. D. Hunter. Matplotlib: A 2D graphics environment. *Computing in Science & Engineering*, 9(3):90–95, 2007. doi: 10.1109/MCSE.2007.55.

Appendix

Species and reaction energies are found in Figures A.1, A.2, and A.3 for LFP, LCO, LMO chemistries respectively.

Figure A.1: Reaction energies and species formation energies from LFP-cathode decomposition.

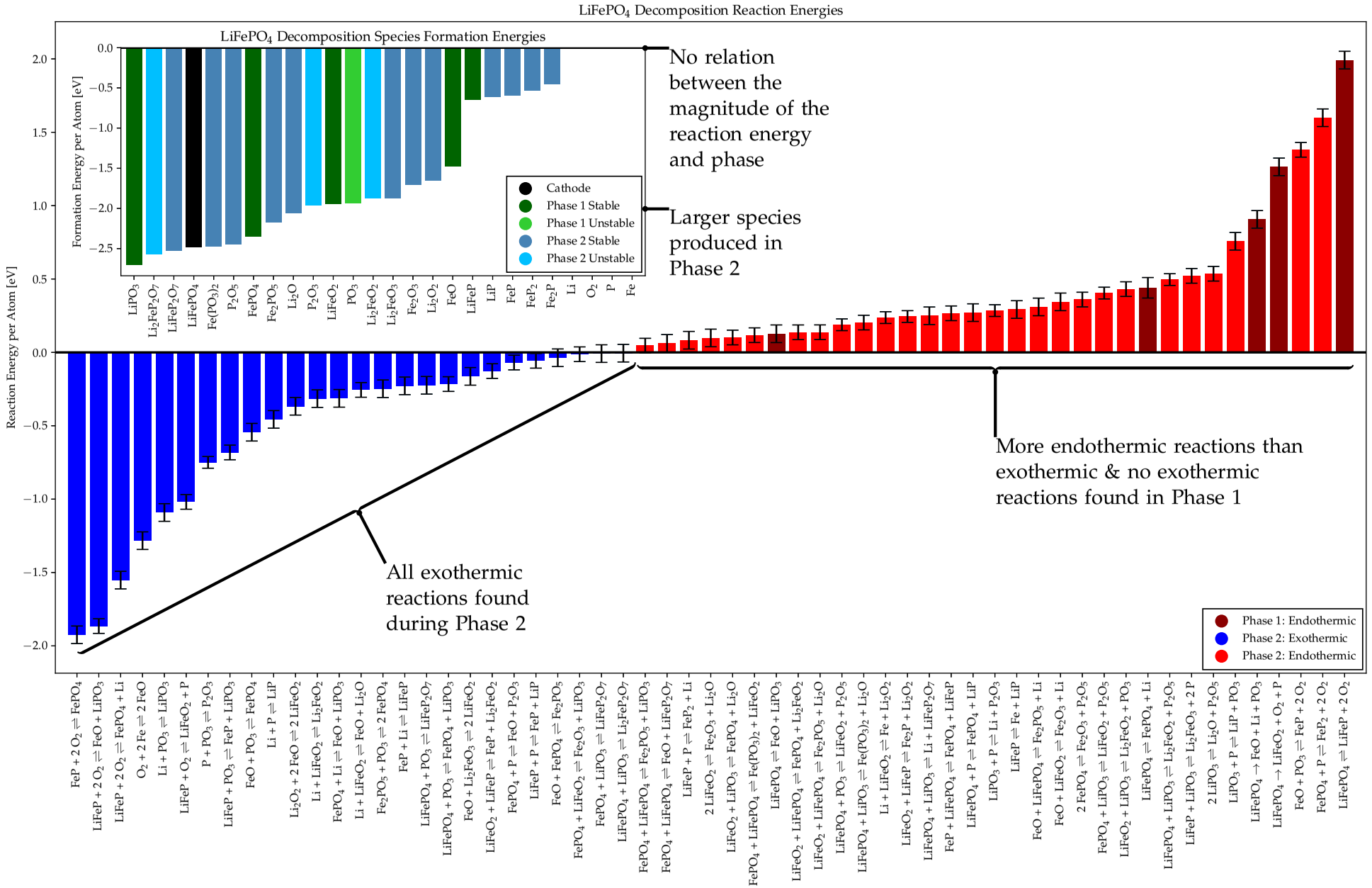


Figure A.2: Reaction energies and species formation energies from LCO-cathode decomposition.

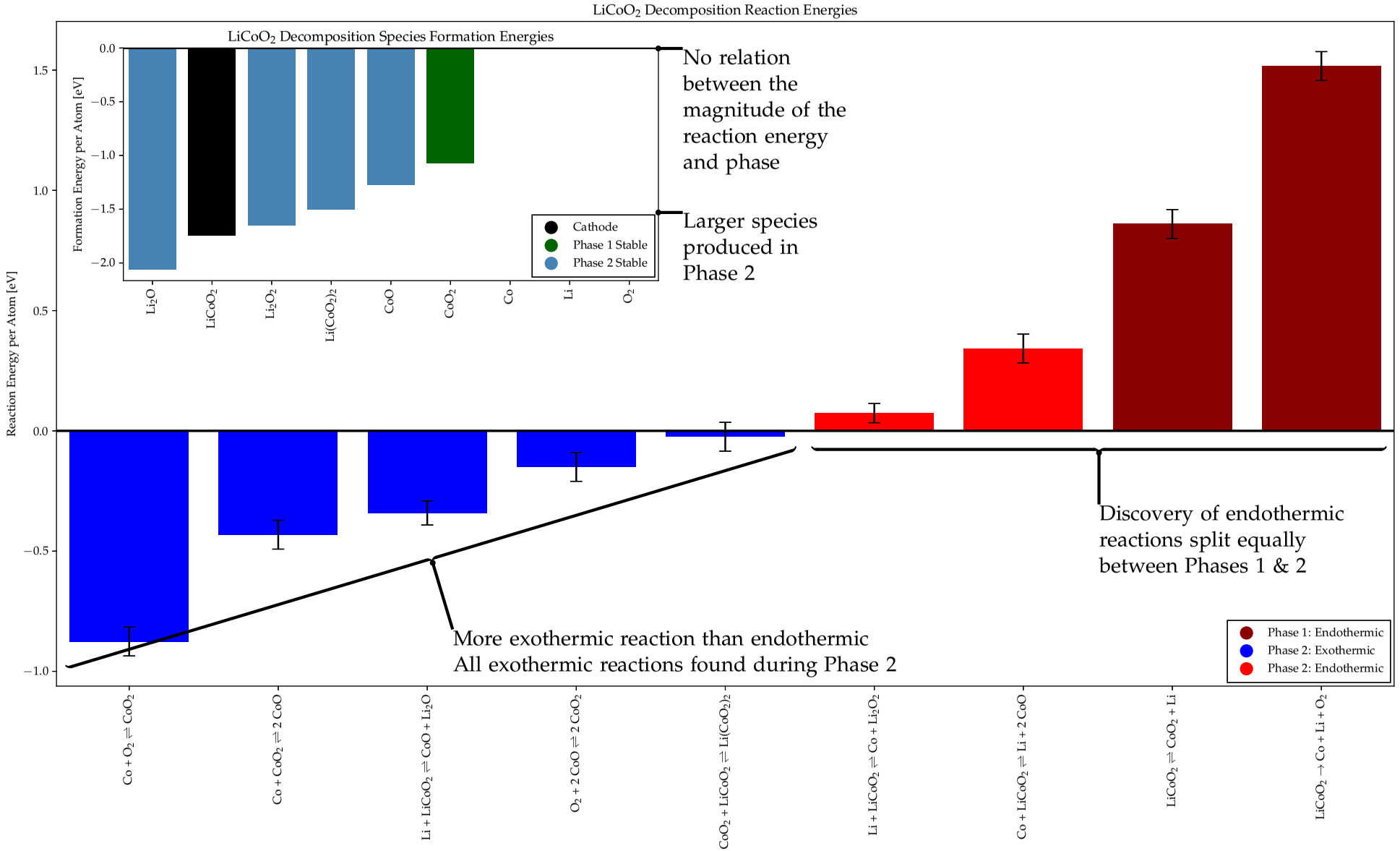


Figure A.3: Reaction energies and species formation energies from LMO-cathode decomposition.

